EPJ Photovoltaics **16**, 17 (2025)

https://doi.org/10.1051/epjpv/2025005

Available online at:
www.epj-pv.org

Special Issue on 'EU PVSEC 2024: State of the Art and Developments in Photovoltaics', edited by Robert Kenny and Gabriele Eder

ORIGINAL ARTICLE OPEN ACCESS

Quantifying the effect of shadow formation on photovoltaic sources under thin object shading: an image analysis approach

Matthew Axisa, Luciano Mule'Stagno, and Marija Demicoli*

Institute for Sustainable Energy, University of Malta, MSD 2080 Msida, Malta

Received: 26 June 2024 / Accepted: 16 January 2025

Abstract. This study aims to quantify the size and intensity of umbra and penumbra shadows on photovoltaic (PV) modules and assess the resulting potential power loss using image analysis techniques. An innovative algorithm, developed from open-source code, was employed to analyze shadow characteristics, alongside outdoor experiments to measure the raw power loss caused by thin objects shading the PV module. Spearman correlation analysis revealed a weak negative correlation between power loss and object distance, which strengthens with increased object thickness. For larger objects between the range of 10 and 16 mm, the raw power loss is predominantly influenced by umbra intensity, while smaller thin objects in the range between 2.8 and 8 mm are affected more by the intensity of the penumbra shadow. Moreover, beyond a distance of 225 cm, for object thicknesses up to 16mm, umbra shadows disappear, leaving only penumbra, which continues to cause power loss, though at a lower intensity. The study's key findings indicate that thicker objects generate stronger umbra shadows, correlating more significantly with power loss, while thinner objects create diffuse penumbra shadows with a reduced impact. Penumbra size and intensity play a critical role, as larger penumbras correspond to a slower reduction in power loss over distance. Shadow intensity, particularly for thicker objects, proves to be a more decisive factor in the raw power loss output than shadow size, as the increase in shadow size compensates for the loss in intensity. The image analysis techniques developed in this work provide an effective method for objectively quantifying the size and intensity of umbra and penumbra shadows, highlighting the importance of shadow dynamics.

Keywords: Photovoltaics / shading / thin object / image analysis / shadow formation

1 Introduction

Photovoltaic (PV) systems have become a pivotal component of the global shift towards renewable energy, with installations worldwide growing at an unprecedented rate. In 2023 alone, the European Union's solar capacity increased by over 60 gigawatts (GW) up to a total of 259.99 GW, accentuating the rapid adoption of this clean energy technology [1]. However, while PV systems commonly refer their capacity with a theoretical peak power, actual performance often falls short due to various limitations. Among these, shading stands out as one of the most detrimental factors. In the realm of shadow formation, by principle a shadow is formed by two distinctively different parts named as umbra and penumbra. These shadows are created when a light source is partially or fully obstructed by an opaque object [2]. Moreover, the umbra is the darkest central part of the shadow, where the light source is entirely blocked, and no light reaches. Surrounding the umbra is the penumbra, a lighter, outer shadow where only a portion of the light is obstructed, allowing some light to diffuse around the edges of the object. This creates a gradient effect from complete darkness in the umbra to partial shading in the penumbra as seen in Figure 1.

Even minor shading from thin objects can disrupt the uniformity of sunlight on PV cells potentially causing output losses [4]. A significant amount of research has been conducted on partial shading with evidence that even minor shading can disrupt current flow through the entire array, leading to greater power loss than the shaded area alone [5,6]. Additionally, shaded solar cells may operate in reverse bias, not only reducing the power generation but also dissipating acting as load, further effecting the output of the subsequent unshaded solar cells connected in series [7]. This abnormal operating instance highlights the importance of understanding and mitigating shading effects to ensure optimal performance. Addressing these challenges is essential to maximize the efficiency of solar

* e-mail: marija.demicoli@um.edu.mt

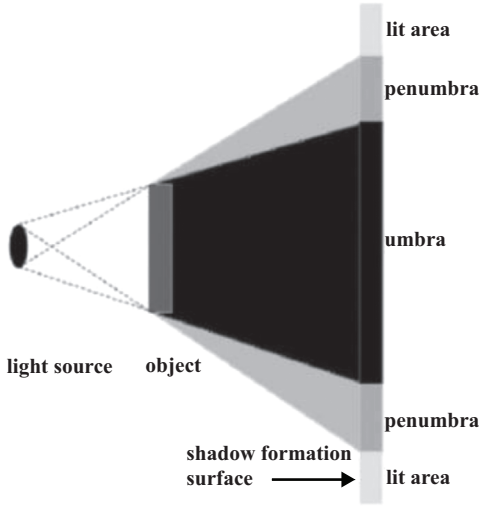

Fig. 1. The principle of shadow formation indicating umbra and penumbra [3].

installations, particularly as the demand for renewable energy continues to grow. Throughout the years, the advancement of image analysis techniques has risen in popularity to identify anomalies and inconsistencies at a given scenario. This approach has also been applied to detect and analyze shading on PVs, enabling more precise and rapid assessments, and thus aiding mitigation strategies. This is especially critical in the context of the United Nations' Sustainable Development Goal 7 (SDG 7), which aims to ensure access to affordable, reliable, sustainable, and modern energy for all. Achieving this goal requires not only the widespread deployment of solar technologies but also the optimization of their performance under real-world conditions.

Image processing is described by Kour et al. as the process of "changing the nature of an image in order to improve its pictorial information for human interpretation, for autonomous machine perception" [8]. Since images are becoming increasingly sharp, detailed, and achievable by most available electronic devices, extrapolating partial shading data has become a possibility. This data would lead to detection of faults, cell hotspots, defects and dust detection amongst other applications [9]. In [10], partial shading on a PV module was detected using an optical camera while [11] took this approach a step further by employing a camera mounted drone to inspect the condition of a large PV plant. Various methods of shading identification exist with one of the most popular being infrared imaging used in applications such as the identification of aging in PV systems as studied by [12,13].

In his study using only a standard single-lens reflex (SLR) camera, Ryad et al. [14] was able to create an algorithm capable of tracking the Global Maximum Power Point (GMPP) by using partial shading detection capable of detecting any shadow transposed on a PV module. The authors use an open-source programming tool to derive a code capable of converting a normal Red, Green, Blue (RGB) image into Hue Saturation Value (HSV) [15]. However, in an early study conducted by Sural et al. [16],

Fig. 2. Shadow cast on a white paper by building [22].

the thresholding analysis was conducted with the more favorable greyscale image rather than HSV. Similarly, the shadow was detected at cell level by the conversion to greyscale, providing the researcher with a number identifier between zero (pure black) and 255 (pure white) and transposed as a matrix. The concept was elaborated upon by Gutiérrez et al. with a methodology that develops a way of identifying at cell level the percentage shadow on each cell on a PV module. This image analysis method enabled the author to analyze the shading ratio; however, it lacks to quantify the intensity of the shadows or distinguish between light and dark shadows [17]. Contrastingly, Rehman et al. distinguished between light and dark shadows by classifying light shading as a solar radiation level of $500\,\mathrm{W/m^2}$, and dark shadow with a very limited light transition of $100\,\mathrm{W/m^2}$ [18]. The commonality among the aforementioned studies is that, even at solar cell level analysis, none have adequately categorized the shadow into the proper optical shadow formations of umbra and penumbra.

Notably, researchers with theoretical knowledge in shadow formation tend to achieve superior results in various image analysis applications. This is evident in Sinha et al.'s study [19] where comprehensive principles of shadow formation, including the classification of and penumbra formations, were applied alongside Otsu Method [19,20] for thresholding to remove cast shadows from images. Additionally, the author identifies various shadow detection methods, including intensity analysis, texture analysis, segmentation, mask construction, color-based, and edge-based approaches. The study concludes that Otsu's method is more effective for shadow removal than for shadow extraction. Furthermore, Dimitros extends Sinha's work [19] by exploring the fuzziness of shadows and identifying shadow border issues within the context of quantum mechanics, which he terms the theory of fuzzy sets, encompassing the broad penumbra of shadows [21]. The same fuzzy shadow cast on a white piece of paper was shown by Huang et al. [22] as seen in Figure 2. Moreover, to detect the shadow boundaries of umbra and penumbra, Huang et al. was able to crop the region of importance as seen in Figure 3 and subsequently plot the intensity of pixels, resembling a sigmoidal curve function. The principle is based on the observation that an umbra shadow maintains consistent intensity, whereas a penumbra shadow contains a multitude of varied intensity levels. As soon as the umbra begins to lose its intensity, it can be classified as a penumbra. By constraining the penumbra shadow, the boundary where the penumbra ends and the

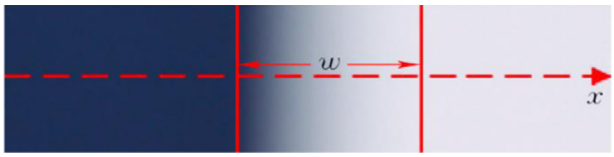

Fig. 3. Shadow boundary where w represents the penumbra region and x depicts the distance of pixels [22].

background value begins, can be accurately determined. Given that the penumbra cannot maintain consistent intensity like the umbra, these features are crucial for delineating shadow boundaries. The sigmodal rule was further elaborated by Giraud-Carrier et al. [23] who used the sigmoidal function as a measure of a classifier that related to the noise called the characteristic transfer function (CTF). The author successfully defines points in the sigmoidal curve that define the range of noise as a measurable performance. The noise can be related to the penumbra where a dynamic shadow intensity is changing which will be the main principal foundation of this study.

Based on the literature reviewed, multiple application of image analysis has been reviewed, with two main research gaps being identified. Firstly, researchers who opt to use image analysis in the field of PVs tend to stop until the shadow edge detection process mainly to eliminate the penumbra shadow and subsequently fail to quantify both the umbra and penumbra shadows. The second research gap pertained to having limited knowledge on how the penumbra correlates with the umbra as variable factors, such as shadow thickness and intensity, vary. Moreover, it is still not understood how the percentage shadow correlates with the loss in power due to the various characteristics of the shadow. Therefore, the primary aim of this research paper is to use image analysis as a methodology to quantify both umbra and penumbra shadows, and to find the correlation between these shadow formations and the loss in power on a PV source. In this way, the study will introduce the adoption of image analysis methods into the realm of PVs to quantify both umbra and penumbra shadows while analyzing their relationship with the power loss.

2 Material and methods

This study employs a two-stage approach to analyze the impact of shadows on power loss in PV systems. The first part is a continuation of experiments conducted in [24], expanding the distance from 25 cm up to 400 cm to acquire a broader dataset and to investigate the effects of lighter penumbra shadows. This phase aims to correlate factors such as the percentage and intensities of umbra and penumbra, with power loss. The objective is to determine whether a relationship exists between these variables and, if so, to quantify the nature of this relationship. The second part involves the application of image analysis techniques to quantify the extent and characteristics of shadows cast on the PV panels and to determine the umbra and penumbra boundaries for a thin object shadow on a PV source. By integrating empirical data with image analysis, this methodology aims to establish a correlation between shadow formation and power loss metrics.

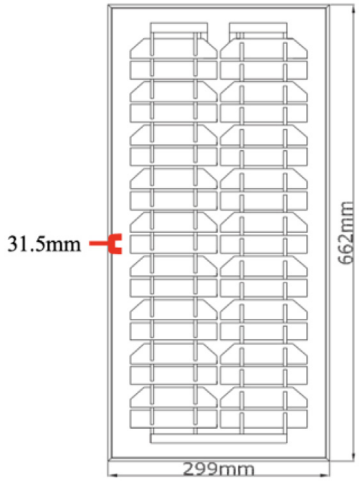

Fig. 4. PV module dimension schematic.

2.1 Power loss experimentation

For the duration of this research article, the term 'thin object shading' refers to any opaque object casting a shadow on a PV module, where the shadow's width (including both umbra and penumbra) does not exceed that of a single solar cell in the PV module. The objective of this power loss experiment is to quantitatively measure the impact of thin object shading on the power output of a small scale PV module, using a fixed resistor as the load. The fixed resistive load aims to contribute as a benchmark to keep the load constant while the distance between the PV module and the shading object is varied and the thickness of the thin object is interchanged independently.

The PV module used in this study is a small-scale PV module (Model No. ET M53620) with a manufacturer-rated power output of 20 watts and overall dimensions of 299 mm in width and 662 mm in length, as shown in Figure 4. This module was chosen due to its large quarter-cut one- diode solar cells having no bypass diode contribution, which allowed for better analysis of thin object shading. Typically, a PV module of this size would have cells cut into even smaller sections, making it difficult to observe the effects of thin object shadows. Moreover, the design of the module consists of 36 quarter-cut solar cells connected in series, with the original solar cell measuring 125×125 mm, as shown in Figure 5. The module consists of multiple individual solar cells, each 31.5 mm in width shown in the schematic diagram in Figure 4. Therefore, the upper limit considered as 'thin object shadow' is given to the shadow in which its total width of umbra and penumbra together do not exceed the width of the solar cell, in this case 31.5 mm. The cast shadow transposed by the thin objects was focused on being horizontal in nature to the PV module as illustrated in Figure 6 and centered directly on two adjacent quarter cut cells. To ensure that

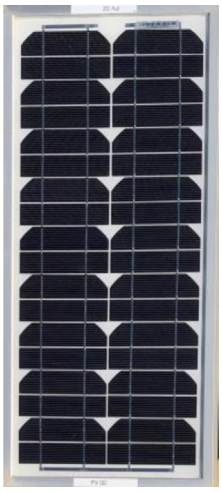

Fig. 5. Experimental PV module.

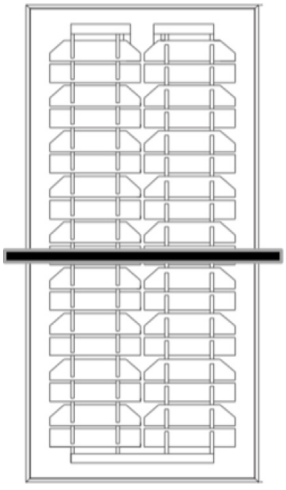

Fig. 6. Transposed thin object shading.

the thin object shading impacts the entire PV module, both sections of the module were covered during testing, as seen in Figure 6.

To better understand and visualize the power loss measured in this study, Figure 7 provides a scientific understanding of partial shading conditions from thin object shading on the experimental PV module chosen, consisting of 36 cells, where 2 of the cells are partially shaded horizontally across the module as previously seen in Figure 6. The explanation uses Kirkoff's Voltage and Current Laws as the fundamental principles for analyzing the electrical circuits. The blue curve corresponds to the ideal case of a fully unshaded PV module which in the case of the experimentation of the study is the curve of the control PV module with the maximum power at the rated load resistance denoted as P_{max} (Unshaded PV). As a conceptual understating the diagram denoted the short circuit current a value of 36 I_{sc}, representing the I_{sc} of the combined 36 cells in series as well as 36 V_{oc} representing the combination of the 36 cells in open-circuit voltage for the control PV module. Moreover, the full 36 cells can be split into the individual characteristic of 34 separate unshaded solar cells represented by an IV (Current and Voltage) curve in green where both the current and voltage are reduced due to the presence of less solar cells in series and the pink curve representing the 2 cells at shaded conditions with a significant reduction in current and voltage level.

The red curve illustrates the case where the module is operating with 34 unshaded cells and 2 shaded cells under thin object shading at a given distance and object thickness. In this case, the current drops significantly more due to the shading-induced mismatch, and the maximum voltage at which the module can operate is also lower. Notably, when the series of unshaded cells are connected in series with the 2 partially shaded ones, the shaded solar cells are forced into reverse bias operation, where they start consuming power instead of generating power due to the full current being generated by the remaining 34 solar cells. The reverse bias occurs when the shaded cells experience a negative voltage because the unshaded cells force current through them and dissipating the power in the form of heat, even though they are not generating power. The reverse bias voltage extends into the negative side of the voltage axis, demonstrating how the shaded cells introduce a reverse voltage in the overall module. Moreover, the furthest reverse bias point on the left side denoted as Point 1 is extended towards the point at which the operating IV curve of the 34 unshaded (visualized in green) and I_{sc} of the 2 shaded solar cells intersect as denoted by Point 2. Therefore, the R_{Load} (Resistive load) connected in series, drawn as a diagonal to the maximum power of the unshaded IV curve P_{max} Unshaded PV, the I_{oper} (operating current) and V_{oper} (operating voltage) of the shaded PV module is representative of the power point the forthcoming experimentation will endeavor to quantify.

Moreover, the power loss expressed as a percentage will be the difference between P_{oper} of the Shaded PV module and the P_{max} of the control PV module. Both PV modules were tested at the Solar Research Laboratory in Marsaxlokk, Malta to verify functionality and acceptable electrical output at the same conditions as documented in Table 1. The calibration process enabled both PV modules to output equal power under corrected Standard Test Conditions (STC) at 25 °C and 1000 $\mathrm{W/m^2}$ irradiance level, essential for accurate and reliable analysis in subsequent experiments. The calibration process was conducted under clear skies, ensuring no partial shading, and both PV modules were thoroughly cleaned beforehand. Each module's power output was recorded every second for a duration of 15 min, allowing for the identification of any mismatch between the modules. A correction factor was then applied to the PV module with the lower output whether from the control or shaded module ensuring the experimentation began on even grounds for accurate benchmarking. Furthermore, the fixed resistive load was crucial to determine the difference in P_{oper} of each thin object shading scenario which will vary across the diagonal of the R_{Load} in accordance with the loss in current corresponding to the severity of shading governed by the umbra and penumbra size and intensity.

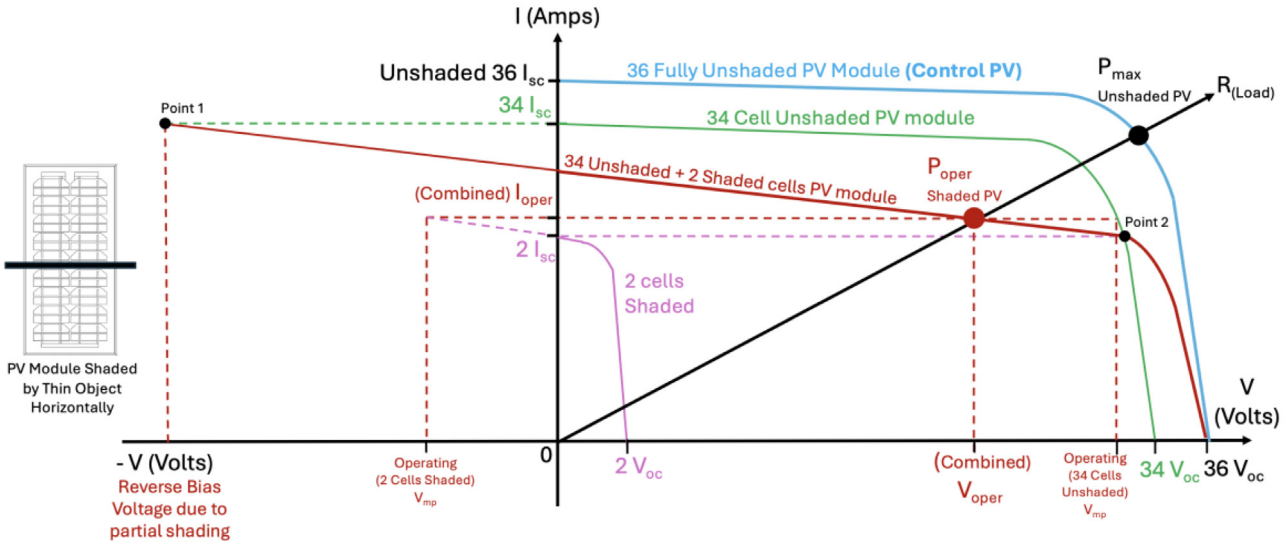

Fig. 7. Cell level partial shading from thin object shading on the experimental PV module consisting of 36 quarter cut solar cells.

Table 1. Electrical characteristics of the solar module used in the power loss experimentation.

Datasheet information	Symbol	Manufacturer datasheet	Tested outdoor calibrated at STC (Control PV module)	Tested outdoor calibrated at STC (Shaded PV module)
Type of Cell Technology		Monocrystalline	Monocrystalline	Monocrystalline
Power Rating	P	20 W	18.91 W	18.81 W
Short circuit current	I_{SC}	1.27 A	1.19A	1.17 A
Open circuit voltage	V_{OC}	21.96 V	20.82 V	20.78 V
Maximum power point current	I_{MPP}	1.14 A	1.06 A	1.06 V
Maximum power point voltage	V_{MPP}	17.82 V	17.77 V	17.75

This research utilizes the standard procedure applied in IEC 60904-1:2020 and IEC 60891:2021, and the sun position geometrical correction factor as detailed in [24]. These techniques are applied to accurately correct power loss by considering the time of day and the shadow size, which is determined by the azimuth at the time of experimentation. This approach ensures consideration and remedial actions of the multiple outdoor experimentation factors essential for a robust comparison. For this study, the power loss experiments were conducted between midday and 2 PM from June 8th to 10th, 2024, with solar noon occurring at 1 PM. During these times, the sun was at its highest point in the sky for the day and near its peak position for the year. The data retrieved from the pyranometer in the weather station was recorded as an average of every 15-minute increments. Similarly, the temperature of the PV module was measured at the same 15-minute intervals using a digital infrared thermometer aimed directly at the PV module. This approach allows the power loss experiment for a single rod thickness to be conducted across all distances up to 400 cm under consistent irradiance and temperature conditions.

To better visualize the outdoor experimentation setup as well as the improvements made to the previous setup [24], Figures 8 and 9 represent the conceptual design and the physical setup of the outdoor experimentation respectively, with the object thickness ranging between 2.8 mm and 16 mm. The setup also includes the capability of varying the distance between the PV source and the shading object up to 400 cm while the Control PV module and the Shaded PV module were situated in close proximity to each other to maintain an equal exposure to outdoor conditions. Moreover, since there is significant range of thin object thicknesses, this study endeavors to classify the thickness into two main categories of small and larger thin objects as the main scope of this research as categorized in Table 2.

2.2 Image analysis tool

The aim of using an image analysis approach is to enable the accurate quantification of percentage umbra and penumbra of thin object shadow instances. The shadow quantification process detailed below was derived

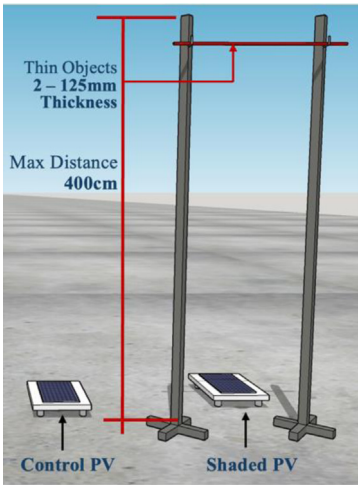

Fig. 8. Conceptual visual of the outdoor methodology.

Fig. 9. As built outdoor experimentation setup.

specifically for quantifying a spectrum of shadow sizes for thin object shading as transposed on a white background. The method being used in this study revolves around the dynamic principal range of pixel values as seen in Figure 10. The dynamic pixel range in digital images spans from 0 (black) to 255 (white). Each pixel value represents an intensity level, with 0 being no light and 255 being maximum light. Values between these extremes represent shades of grey, allowing for 256 distinct intensity levels. This range enables a detailed representation of visual information in greyscale images, simplifying analysis by focusing on light and dark variations.

The image analysis process begins with the user loading an image into the image analysis tool. Once the image is loaded, it is automatically converted from an RGB image to a greyscale format, simplifying the analysis by focusing exclusively on the intensity values. In this study, RGB images were converted to greyscale to facilitate the computational efficiency of shadow detection without compromising accuracy. Although greyscale conversion removes chromatic information, the approach used in this study is focused on luminance-based shadow detection by using Pythons's 'Pil' (Pillow) library, which is inherently robust to the absence of color data. Shadows primarily manifest as intensity gradients rather than chromatic shifts, particularly in outdoor environments where lighting conditions are the dominant factor in shadow formation. Prior research by Chandran et al. and Kumar et al. [25,26] has demonstrated that intensity-based methods perform comparably in both greyscale and RGB contexts, especially when shadow boundaries are defined by luminance differences. Therefore, the greyscale conversion did not impede the algorithm's ability to accurately detect shadows, even in the presence of complex shadows on a white surface without any background texture for simplicity of analysis.

From the greyscale image, an average pixel intensity column is obtained by calculating the average intensity for each column of pixels in the image. The darkest pixel within this average intensity column is then identified, serving as a reference point for subsequent normalization. Normalization is carried out by assigning a value of 1 to the darkest pixel and 0 to the lightest pixel, effectively rescaling the intensity values between these two extremes. A dual mirrored sigmoidal curve is then plotted using these normalized intensity values as depicted in Figure 11. This graph provides a visual representation of the umbra and penumbra regions, with a high peak curve indicating a smaller umbra region while a wide peak representing a larger umbra region. Two sigmoidal curves are fitted to the data, shown as the blue plot.

To determine the start and end points of umbra and penumbra respectively, this study employes the method previously used by Mirylenka et al. [27] where the active noise range induces a measurable change in the performance as shown at the curvature points of the sigmoidal curves. Therefore, for the case of our study, the noise level can be said to be equivalent to the penumbra shadow since using the applied criteria it is the only shadow formation that has a dynamic change in shadow intensity. On the other hand, umbra shadow has a constant intensity throughout since no light passes through the opaque thin object. Therefore, as highlighted by Mirylenka et al. [27] while deriving the sigmodal rule framework the top and bottom 0.05 normalized measure of distance values from optimal dark intensity are selected as cut-off points for the penumbra value. These values are indicated in Figure 12 by Points A and B for the left-side sigmoidal curve and Points C and D for the right-side sigmoidal curve. From these selected values, four key points on the dual sigmoidal curve are identified: the points where the penumbra ends and starts both above and below the midpoint. To gain a more comprehensive understanding of the range selected by the algorithm for the start and end points of the umbra and penumbra, Tables 3 and 4 describe the conditions at which these points have been derived including the corresponding points A-D indicated shown in Figure 12. These points are marked with distinct colors (red, green, black and purple) and their corresponding denormalized Y values are extracted to a comprehensive data file.

Table 2. Shading object thicknesses as categorized for the purpose of correlation in this work.

Category 1–Small thin objects				**Category 2** – Larger thin objects			
2 mm	3.2 mm	6 mm	8 mm	10 mm	12 mm	14 mm	16 mm

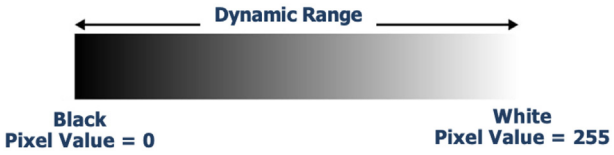

Fig. 10. Dynamic range of greyscale pixel intensities.

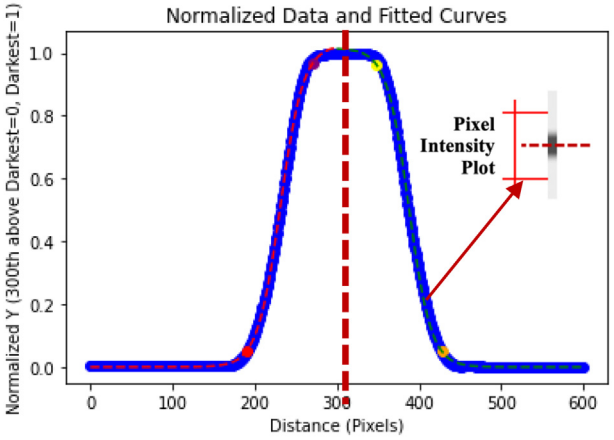

Fig. 11. Typical shadow intensity plot.

The analysis considers two scenarios: one where both umbra and penumbra are present and another where only penumbra is present. The boundaries for these scenarios are derived based on the denormalized values. Example values are calculated to illustrate these boundaries. Pixel counts are then determined for each category (above and below the identified points) and the total pixel count for each category is calculated. The percentage of pixels in each category is obtained by dividing the pixel count by the total number of pixels in the averaged column.

A scenario is defined as 'Only Penumbra' if the difference between the darkest pixel and either Point B or Point C is less than or equal to 3-pixel value, indicating a minimal or no umbra presence. This value was found through an extensive exercise of analyzing 240 images to categorize which of these have only penumbra shadow formation. These images consisted of an overall pixel dimension of 1708 × 3574 with an accuracy of pixels of ±68 pixels which are attributed to the cropping aspect of the image to focus on the PV module. To maintain consistency in image capture, all photos were taken with a Canon EOS 6D Digital SLR using manual settings of ISO 200, an aperture of f/3, and a shutter speed of 1/200, ensuring high-quality results. Additionally, environmental data from a nearby weather station at the time of capture

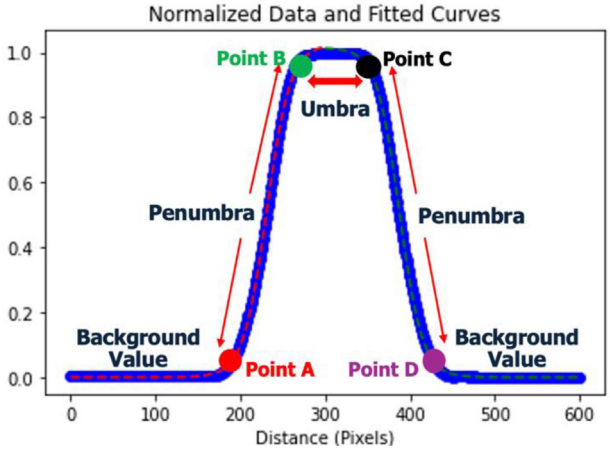

Fig. 12. Sigmoidal curve fitting and noise point identification.

indicated clear skies with no partial shading from clouds. A detailed data collection procedure as well as the equipment used can be found in [23]. The average solar global radiation was 964 W/m^2 between one hour before and after solar noon (1 PM) at the Institute of Sustainable Energy in Marsaxlokk, Malta (Latitude: 35°50′03.42″N, Longitude: 14°32′36″E).

As already highlighted, by principle, umbra shadow should have a constant intensity value, and in the case where there is only penumbra, no umbra should be present. This situation is detected by the image analysis tool since the latter first attempts to quantify the umbra shadow but since the top of the sigmoidal curve resembles a high peak with no plateau as seen in the difference between Figures 13 and 14, the three normalized pixel value discrepancy between the darkest pixel and the end of the noise level will trigger the tool to consider the instance as one with only penumbra shadow. The results, indicating whether both umbra and penumbra are present or only penumbra is detected, are determined based on this analysis. Moreover, the process of the image analysis tool methodology can be seen graphically in the flow chart in Figure 15.

3 Results and discussion

The algorithm described in the previous section and outlined in Figure 15 was translated into an open-source code using Python v3.12.2 and a graphical user interface (GUI) enabled ease of illustrating graphs and resulting figures as seen in Figure 16. All 128 images, including small and large thin shading objects, comprising of 8 different thicknesses and 16 distances between 25 and 400 cm at an increment of 25 cm were analyzed and the resulting umbra and penumbra values where documented. Figures 17 and 18

Table 3. Determining the start and end points in the instance where the image contains both umbra and penumbra shadow.

	Left Sigmoidal Curve		+	Right Sigmoidal Curve	
	Start	**End**		**Start**	**End**
Umbra	Darkest Pixel	Point B		Darkest Pixel	Point C
Penumbra	Point B + 1 Pixel	Point A		Point D + 1 Pixel	Point D

Table 4. Determining the start and end points in the instance where the image contains only penumbra shadow.

	Left Sigmoidal Curve		+	Right Sigmoidal Curve	
	Start	**End**		**Start**	**End**
Penumbra Only	Darkest Pixel	Point A		Darkest Pixel	Point C

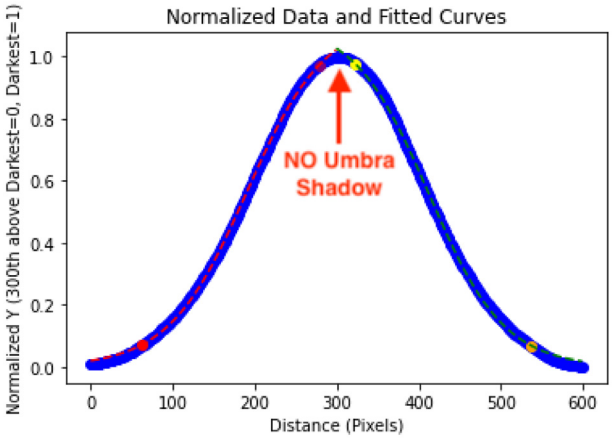

Fig. 13. Normalized shadow intensities given by the image analysis tool – instance indicated no umbra shadow due to the presence of the peak (no plateau).

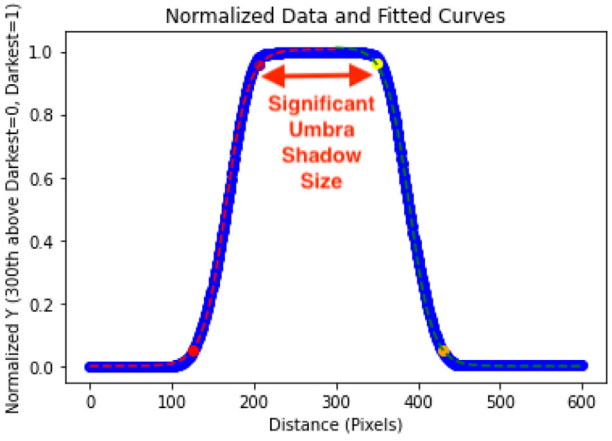

Fig. 14. Normalized shadow intensities given by the image analysis tool – instance indicating a significant amount of umbra shadow.

illustrate a sample image dataset for thin object categories analyzed at various distances between 25 cm and 400 cm. At first glance, the contrast between shadow intensity and formation is clearly evident between the small and large thin objects, the correlation of which will be discussed hereafter.

3.1 The quantifiable effect of various sized thin object shading on a PV module

Figure 19 illustrates the quantifiable effects of thin object shading on a PV module, categorized and differentiated by various point markers on the graph. Notably, power loss was not recorded beyond a 400 cm distance for all shadow thicknesses because, in some cases, the total umbra and penumbra exceeded the width of the solar cell. This caused the penumbra to spill onto the cells above and below the selected row, introducing additional mismatch losses, which prevented a fair basis for comparison.

The analysis of thin object shadows on the PV module reveals several critical insights. For thin objects measuring 2.8 mm and 3.2 mm in thickness, power losses remained within the margin of error less than 1.5% for all distances tested indicating a negligible impact. This minimal power loss is attributed to the low intensity of the shadows cast by these smaller objects, as well as the relatively limited size of the shadow compared to the overall PV module, where the shadow is primarily in a penumbra-dominated region. Interestingly, between 25 cm and 150 cm distances, power loss remains relatively constant and linear. However, beyond 175 cm, larger-sized thin objects begin to show a slight linear decline in power loss, while for smaller thin objects, this decline is observed much later, around 275 cm. Therefore, the linearity in power loss over most of the distance range suggests that, even as the object moves further from the PV module, the shading effect retains much of its impact. Additionally, the linearity indicates that, although the overall shadow intensity decreases with

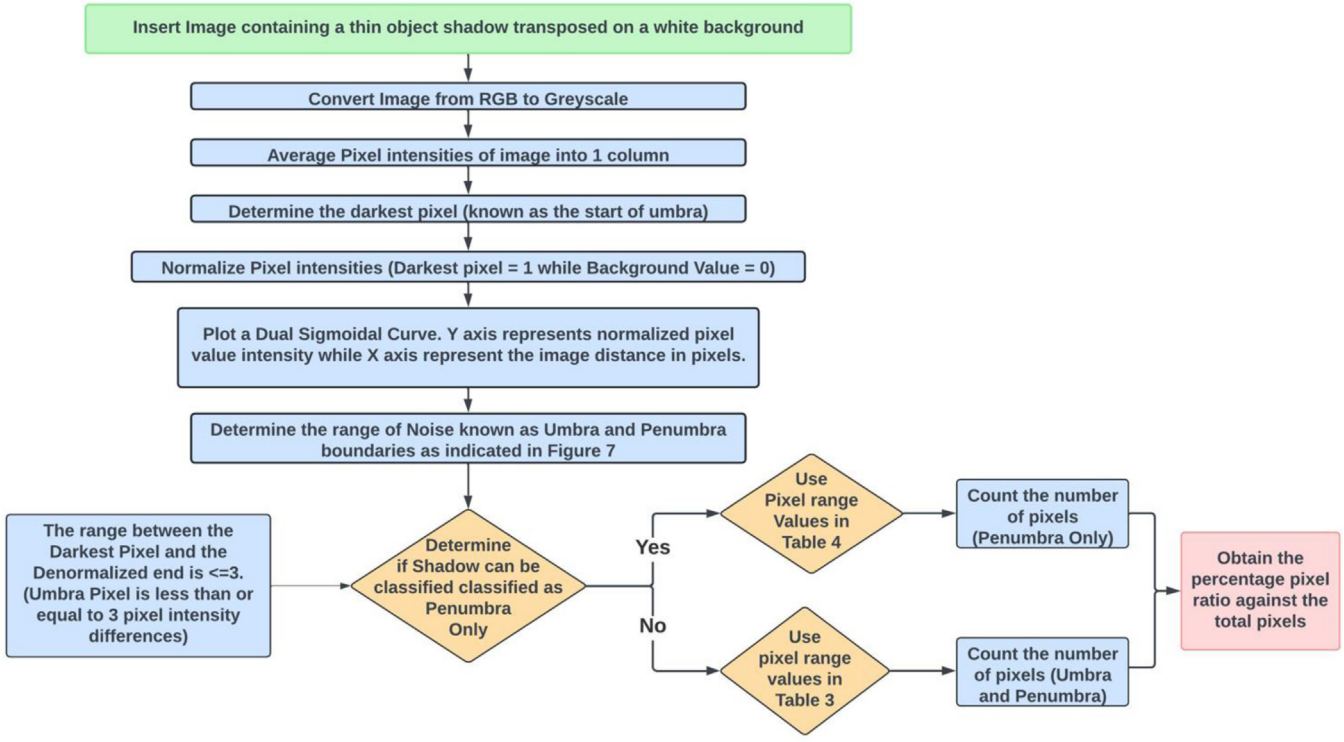

Fig. 15. The shadow quantification algorithm based on key literature points identified in Section 1.

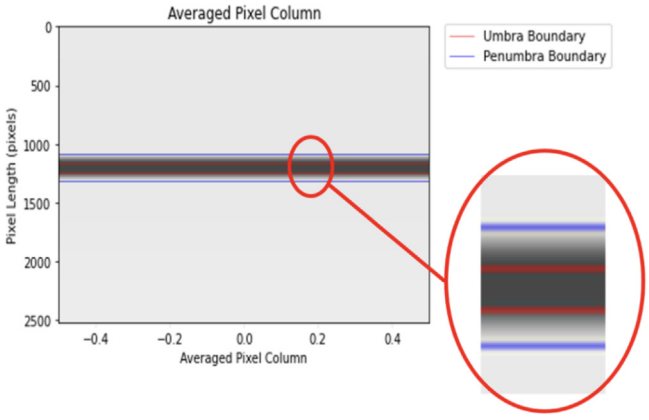

Fig. 16. Resulting image of the image analysis tool deriving the percentage umbra and penumbra based on the methodology described in Section 2.

increasing distance, the growing penumbra size compensates for most of the loss in intensity by increasing the overall shadow size.

Furthermore, future research could explore these trends in more detail, particularly to determine the exact points where thin object shading becomes negligible. This could involve extrapolating the power loss data to insignificant levels to identify the distance at which the effect of each thin object on power loss can be considered minimal. Another key takeaway from the results in Figure 19 is that a 16 mm thin object produces a shadow that is twice its width even at only 225 cm away. This is due to the fact that, at 250 cm, the overall shadow exceeds the solar cell width of 31.5 mm. Consequently, the combination of umbra and penumbra covering the entire solar cell results in approximately a 42% loss in power output, with nearly an even split between the umbra and penumbra shadow sizes.

3.2 Correlation analysis of power loss with distance, thickness, umbra/penumbra size and intensity

To examine the relationships between power loss and various influencing factors, this research employs the Spearman correlation matrix. Spearman correlation, a non-parametric measure, evaluates the strength and direction of monotonic relationships between variables. It was chosen over Pearson correlation due to its robustness against outliers and its suitability for non-normal data distributions, making it more appropriate for analyzing complex interactions in the data. The primary focus is on the relationship between power loss and factors such as size, umbra intensity, penumbra intensity, and distance, as illustrated in Figure 20. Two Spearman correlation matrices have been generated for two categories of thin objects, with raw shading power loss being the primary dependent variable of interest. Additionally, the study adopts the correlation coefficient metric proposed by Hair et al. [28] to quantify the relationships between the identified factors as seen in Table 5.

The analysis of the correlation between power loss and distance reveals an overall weak relationship for both categories of object thickness. However, the correlation becomes stronger as the object thickness increases. The negative correlation coefficient for distance indicates that as the distance between the thin object and the PV source

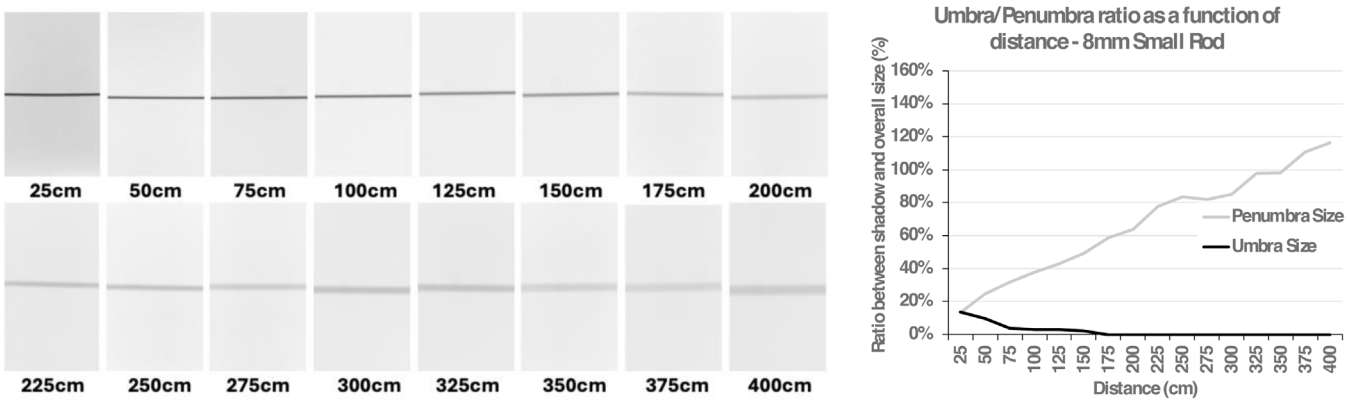

Fig. 17. Sample dataset illustrating image analysis performed on a small thin object (8 mm).

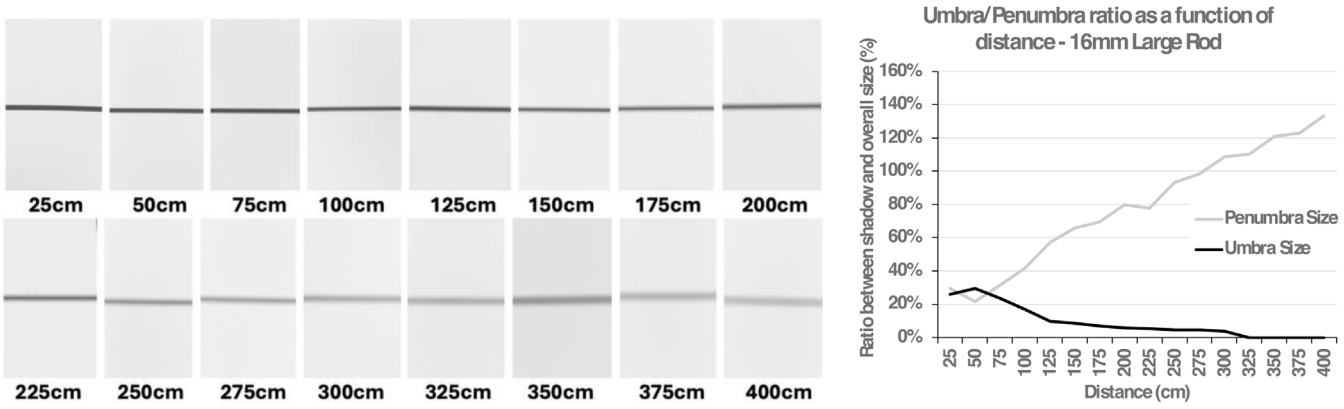

Fig. 18. Sample dataset illustrating image analysis performed on a large thin object (16 mm).

increases, power loss decreases. This trend is evident in Figure 18, where the shadow shifts from a high-intensity umbra to a more diffuse penumbra at greater distances, thereby reducing the overall shadow intensity and associated power loss.

The correlation between power loss and the size of the penumbra strengthens as the object thickness increases, though it remains weak overall. The negative correlation suggests that an increase in penumbra size corresponds to a decrease in power loss, likely because a larger penumbra occurs at greater distances where the higher-intensity umbra diminishes. While the impact of penumbra size on power loss is limited, other factors, such as penumbra intensity, play a more significant role, particularly for smaller, thinner objects. This is evident from the stronger negative correlation between penumbra intensity and power loss compared to penumbra size, highlighting the crucial influence of shadow intensity on power loss. Furthermore, the analysis shows that as thin objects increase in diameter, the correlation between penumbra intensity and power loss weakens, while the correlation with umbra intensity increases. This is mainly due to thicker objects casting more substantial umbra shadows.

The image dataset demonstrates that umbra shadows are either absent or occupy only a small percentage of the shadow area for smaller, thinner objects. In contrast, larger, thin objects consistently cast umbra shadows due to their greater thickness. Interestingly, the correlation between power loss and umbra intensity varies with object thickness: for smaller objects, there is little to no correlation, largely because umbra shadows are rare in these cases, whereas for thicker objects, the correlation is weakly negative. The analysis of the image dataset indicates that umbra intensity for smaller objects is highly variable and constitutes less than 10% of the cell size in the majority of cases. Although the power loss dataset was limited to points where the overall shadow exceeded the solar cell on the PV module, the image dataset extended up to 400 cm in all instances to observe the expected umbra and penumbra size and intensity trends. A key observation from the extended imagery is the significant, continuous increase in penumbra value for thinner objects, while the dominance of umbra shadows becomes more apparent in larger, thin objects. This trend suggests that as the thickness of the shadow increases, both the intensity and size of the umbra grow. Future studies should further

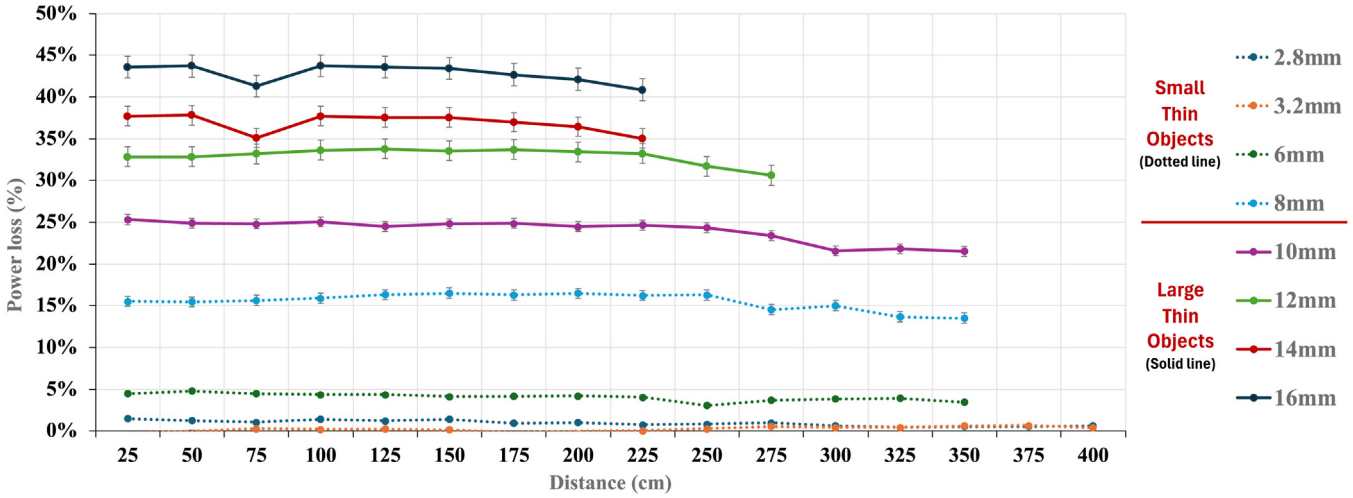

Fig. 19. Analyzing the various power loss levels as the distance between the two categories of thin objects and the experimental PV module increases.

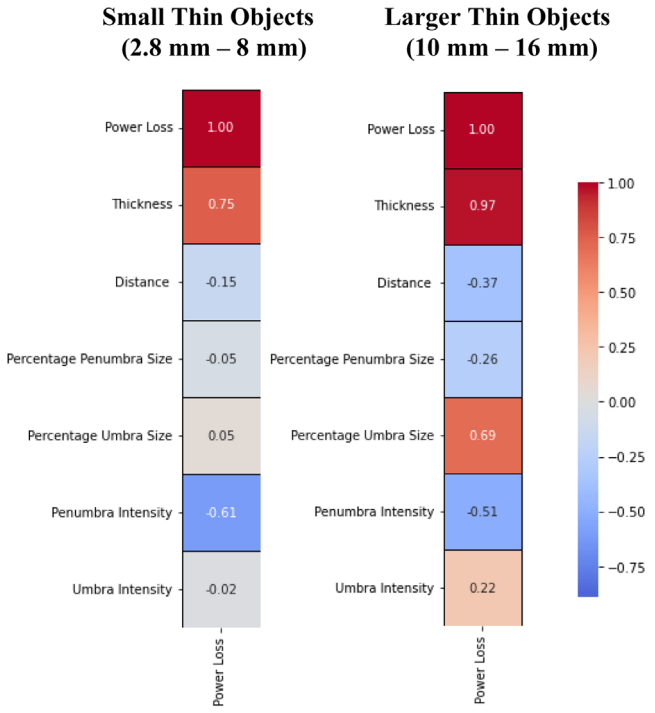

Fig. 20. Spearman correlation matrix for small and large thin objects respectively assessing all dependent and independent factors.

Table 5. Correlation coefficient metric [28].

Size of correlation	Interpretation metric
0.91 to 1.00 / −0.91 to −1.0	Very strong
0.71 to 0.90 / −0.71 to −0.90	High
0.41 to 0.70 / −0.41 to −0.70	Moderate
0.21 to 0.40 / −0.21 to −0.40	Weak
0.20 to 0.01 / −0.20 to −0.01	Very Weak

investigate the interplay between penumbra size and intensity in greater detail to provide a deeper understanding of the overall impact of penumbra shadows.

3.3 Analyzing the size of umbra and penumbra as distance increases from 25 to 400 cm

In this section, the size of the umbra and penumbra at each object thickness and distance will hereon be analyzed as determined by the analytical method detailed in Section 2.2 of the methodology in this research article. These sizes were calculated as a percentage of the total length of the solar cell, which in this case is 31.5 mm, corresponding to the quarter-cut cell design. As indicated in Figure 21 the upper threshold represents 100% coverage of the solar cell. Values exceeding this threshold suggest that the combined umbra and penumbra shadow extends beyond the width of the solar cell, thus spilling over onto adjacent cells above and below the focal solar cell. However, this study focuses specifically on the effects observed on a single solar cell. Consequently, any power loss associated with shadow spillover beyond 100% coverage has been omitted from the analysis.

For the range of thin objects measured, 2.8 and 3.2 mm in thickness, virtually no umbra shadow was observed on the quarter-cut solar cell within the PV module. Additionally, for all small and thin objects in the range depicted in Figure 21, no umbra shadow was detected at distances beyond 225 cm from the PV module. This suggests a dominant presence of penumbra shadow, consistent with the strong correlation noted in previous observations. Furthermore, at distances exceeding 350 cm, the penumbra shadow reaches a size comparable to that of the solar cell itself, indicating that the cell is entirely covered by penumbra shadow. As observed in the power loss analysis, at these distances, the reduction in light intensity due to penumbra shadowing is partially offset by the increase in shadow size, resulting in a nearly linear and consistent power loss, with only a slight decrease in intensity. Moreover, based on the conditions and methodology of

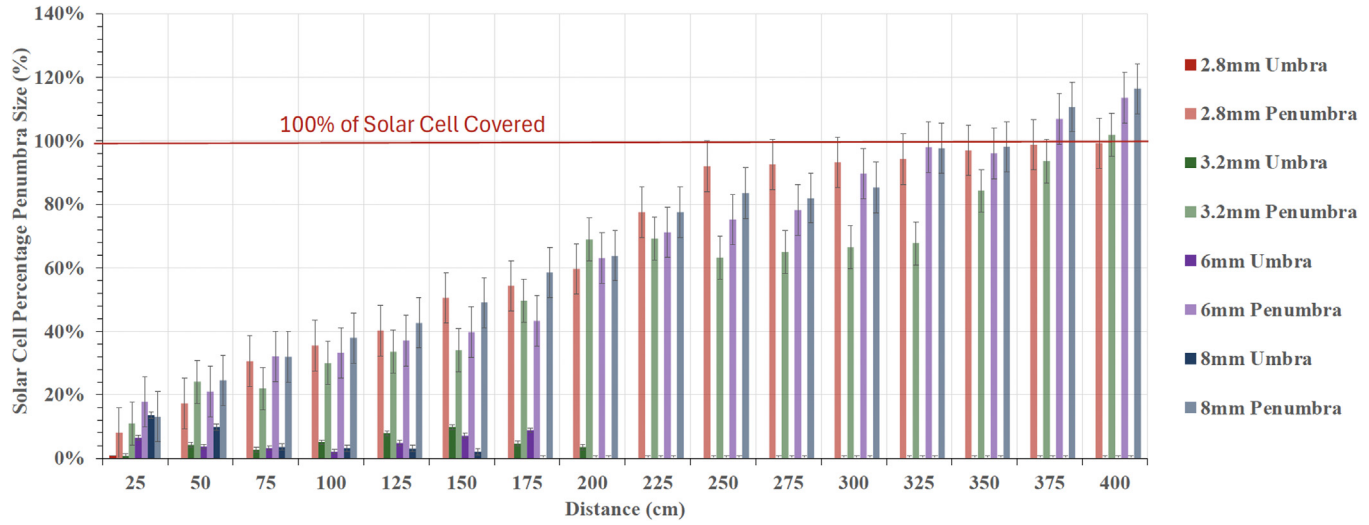

Fig. 21. Comparative graph of the umbra (dark color) and penumbra (light color) shadow size as a percentage of the quarter cut solar cell for small thin objects ranging from 2.8 mm − 8 mm in thickness versus the distance from the PV module.

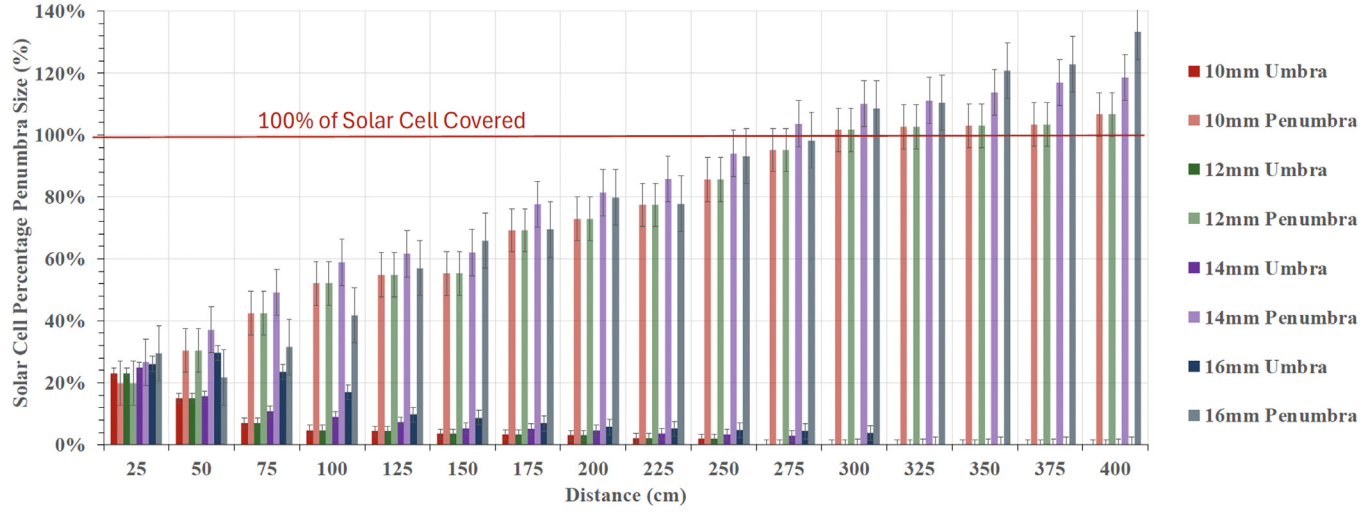

Fig. 22. Comparative graph of the umbra (dark color) and penumbra (light color) shadow size as a percentage of the quarter cut solar cell for small thin objects ranging from 10 mm − 16 mm in thickness versus the distance from the PV module.

this study, where the resistive load was held constant and only the distance between the PV module and the shading object was varied, we observe that the increase in shadow size compensates for the reduction in light intensity. This leads to a sustained, although detrimental, power loss, even in the absence of umbra shadowing at greater distances.

The same analytical procedure applied to the large thin object in Figure 22 was conducted as previously described for the smaller thin objects in Figure 21. At a distance of 25 cm, a strong presence of umbra shadow is observed for the larger thin objects; however, this intensity decreases with increasing distance. By 300 cm, all large thin objects exhibit no detectable umbra shadow and are predominantly composed of penumbra shadow.

Interestingly, although the 16 mm thickness is double that of the 8 mm thickness, the overall penumbra shadow observed at distances of 350 and 400 cm was strikingly similar. This suggests that the size of the penumbra shadow does not vary exponentially with the dimensions of the thin object; rather, it remains relatively constant at greater distances. This consistency can be attributed to the faint nature of the penumbra, which may not be adequately captured by the image analysis algorithm. A similar linear effect is noted for the larger thin objects, particularly up to a distance of 150 cm. Beyond this point, however, there is a slight decrease in power loss, indicating that the umbra shadow is gradually being replaced by the penumbra shadow. In conclusion, even though larger objects only cover approximately 30% of the solar cell at a distance of 25 cm from the PV module, this coverage yields an effect comparable to a 100% penumbra shadow, characterized by significantly lighter intensity, as demonstrated by the correlation depicted in Figure 20.

4 Conclusion

This research has the potential to contribute and integrate into the design of PV systems, specifically under thin object shading conditions. The vast majority of current commercially available software primarily estimates thin object shading based solely on the size of the full shadow. However, this study establishes a more scientific approach to quantifying thin object shading by providing a relationship between shadow size and distance, as well as the raw power loss effect, which can be utilized in preliminary design procedures. These procedures indicate that thin objects with a thickness of 3.2 mm or less produce negligible power loss, especially when positioned 200 cm away from the PV source. Moreover, the correlation between these factors enables PV technicians to identify the most significant variables based on the object's thickness. This study concludes that for thin objects ranging from 2.8 mm to 8 mm in thickness, penumbra intensity has the highest correlation with power loss. Therefore, reducing penumbra intensity by increasing the distance of the object from the PV source will help minimize power loss. For larger thin objects, specifically those between 10 mm and 16 mm in thickness, umbra size is more closely correlated with power loss. As indicated by the results shown in Figure 22, relocating the shadow to the point where the umbra transitions to penumbra can further reduce power loss from the PV source.

Interestingly, this research also reveals that the overall penumbra size does not necessarily reflect the original size of the thin objects; for example, the penumbra observed at 400 cm is quite similar to that of a 16 mm object. This phenomenon can be attributed to the rapid decrease in intensity and a corresponding diffusion into the background value. Additionally, while the overall size of the shadow can double, resulting in a reduced intensity, this does not imply that the resultant power loss is greater. The increase in shadow size compensates for the loss in intensity. Thus, even when the thin object is moved away from the PV source, the raw power loss effect retains its detrimental impact up to 150 cm, with a gradual decrease observed thereafter. This consideration is crucial during the design stage of PV systems, and this research enhances the understanding of the dynamics of umbra and penumbra shading on the raw effect of a PV source.

5 Limitations

The limitation of this study is the adoption of a fixed resistive load, which was crucial for maintaining constant electrical factors while allowing for a focused examination of the effects of varying distance or object thickness independently. In a more realistic PV operating environment, where Maximum Power Point Tracking (MPPT) systems dynamically adjust the load to optimize energy capture, the interaction between shading effects and varying loads could lead to different performance outcomes. Furthermore, although the irradiance and module temperature were measured during the calibration process, an ideal scenario would involve using a full-size PV module solar simulator with a reference cell to enhance the accuracy of the calibration under STC conditions. Additionally, the research did not fully account for solar spectrum mismatch correction, which could introduce minor variations in the reported power output. This mismatch occurs when the sunlight spectrum during testing differs from standard conditions, potentially leading to deviations in the corrected power output.

A further limitation of this study lies in the decision to assign a single, averaged intensity value to the penumbra for the sake of simplification, despite the fact that the penumbra displays a dynamic range of intensities resulting from variations in light diffusion at the shadow's edges.This decision was made to streamline the analysis and ensure consistency across the dataset. However, it may result in a loss of granularity, as subtle variations in the penumbra's intensity were not fully captured, which could potentially affect the precision of shadow-related measurements and interpretations.

6 Future works

Building on the findings and limitations of this study, future research could explore additional orientations of thin object shading, such as vertical and diagonal, to enhance the dataset of raw effects. Furthermore, with advancements in PV module design which include the use of different substrings, increased bypass diodes, and innovative maximum power point tracking (MPPT) algorithms subsequent studies could apply the results of this research to develop various strategies for mitigating thin object shading in full-scale PV modules. Moreover, while in this research, a small-scale experimental module was used, the detailed methodology provides the necessary information to adopt such a methodology into a full-size commercial PV module. This approach would help in further applying the findings to full-scale PV systems and translating the raw shading effects to more realistic scenarios.

Acknowledgments

The authors express gratitude for the technical assistance from Mr. Terence Cilia and Mr. Paul Bonnici for their help in constructing the steel structure, administrative support from Mr. Aaron Grech, the provision of weather data by Prof. Ing. Charles Yousif, and the provision of data logging devices from Dr. Ing. Ryan Bugeja.

Funding

This research was funded by the University of Malta research funds.

Conflicts of interest

The authors declare no conflict of interest and have nothing to disclose.

Data availability statement

The data from this study can be obtained by contacting the corresponding author, however, they are not publicly accessible because they are part of ongoing research for a Ph.D thesis.

Author contribution statement

Conceptualization, M.A., L.M., and M.D.; methodology, M.A., L.M., and M.D.; validation, M.A., M.D., and L.M.; investigation, M.A., L.M.; formal analysis, M.A., L.M., and M.D.; resources, M.A., L.M., and M.D.; writing—original draft preparation, M.A.; writing—review and editing, L.M. and M.D.; supervision, L.M. and M.D.; project administration, L.M. and M.D. All authors have read, reviewed, discussed and agreed to the published version of this publication.

References

1. Solar energy (Key facts on solar capacity). Available: https://energy.ec.europa.eu/topics/renewable-energy/solar-energy_en [accessed: Jun. 03, 2024]
2. Z. Liu, K. Huang, T. Tan, L. Wang, Cast Shadow Removal with GMM for Surface Reflectance Component, in *18th International Conference on Pattern Recognition (ICPR'06)* (2006), pp. 727–730. https://doi.org/doi:10.1109/ICPR.2006.357
3. S. Murali, V.K. Govindan, S. Kalady, A survey on shadow detection techniques in a single image, Inform. Technol. Control. **47**, 75 (2018). https://doi.org/doi:10.5755/j01.itc.47.1.15012
4. M.A.A. Mamun, M. Hasanuzzaman, J. Selvaraj, Experimental investigation of the effect of partial shading on photovoltaic performance, IET Renew. Power Generat. **11**, 912 (2017). https://doi.org/doi:10.1049/iet-rpg.2016.0902
5. D. Sera, Y. Baghzouz, On the impact of partial shading on PV output power, in *18th International Conference on Pattern Recognition (ICPR 2006), 20-24 August 2006* (Hong Kong, China, 2008)
6. Z. Wang, N. Zhou, L. Gong, M. Jiang, Quantitative estimation of mismatch losses in photovoltaic arrays under partial shading conditions, Optik **203**, 163950 (2020)
7. E. Özkalay, F. Valoti, M. Caccivio, A. Virtuani, G. Friesen, C. Ballif, The effect of partial shading on the reliability of photovoltaic modules in the built-environment, EPJ Photovolt. **15**, 7 (2024). https://doi.org/doi:10.1051/epjpv/2024001
8. A. Kour, V.K. Yadav, V. Maheshwari, D. Prashar, A review on image processing, Int. J. Electr. Commun. Computer Eng. **4**, 2278 (2012)
9. A. Salazar, E.Q. Macabebe, Hotspots detection in photovoltaic modules using infrared thermography, MATEC Web Conf. **70**, 10015 (2016)
10. S. Salamanca, P. Merchan, I. Garcia, On the detection of solar panels by image processing techniques, in *2017 25th Mediterranean Conference on Control and Automation (MED)* (Valletta, Malta, IEEE, 2017), pp. 478–483
11. C. Henry, S. Poudel, S.-W. Lee, H. Jeong, Automatic detection system of deteriorated PV modules using drone with thermal camera, Appl. Sci. **10**, 3802 (2020). https://doi.org/doi:10.3390/app10113802
12. P.A.A. Pramana, R. Dalimi, Hotspot detection method in large capacity photovoltaic (PV) farm, IOP Conf. Ser.: Mater. Sci. Eng. **982**, 012019 (2020)
13. S.G. Monicka, D. Manimegalai, M. Karthikeyan, R. Gunasekari, Image processing based hot-spot detection on photovoltaic panels, Int. J. Intell. Syst. Appl. Eng. **11**, 510 (2023)
14. A.K. Ryad, A.M. Atallah, A. Zekry, An accurate partial shading detection and global maximum power point tracking technique based on image processing, Eng. Rev. **42**, 46 (2022). https://doi.org/doi:10.30765/er.1636
15. J.-P. Villegas-Ceballos, M. Rico-Garcia, C.A. Ramos-Paja, Dataset for detecting the electrical behavior of photovoltaic panels from RGB images, Data **7**, 82 (2022)
16. S. Sural, G. Qian, S. Pramanik, Segmentation and histogram generation using the HSV color space for image retrieval, in *Proceedings. International Conference on Image Processing* (2002) pp. II-II. https://doi.org/doi:10.1109/ICIP.2002.1040019
17. A. Gutiérrez Galeano, M. Bressan, F. Jiménez Vargas, C. Alonso, Shading ratio impact on photovoltaic modules and correlation with shading patterns, Energies **11**, 852 (2018)
18. H. Rehman et al., Neighboring-pixel-based maximum power point tracking algorithm for partially shaded photovoltaic (PV) systems, Electronics **11**, 359 (2022)
19. A. Sinha, Comparison of techniques used in shadow detection in an image, Int. J. Image Process. Comput. Vis. **8**, 178 (2020)
20. J. Yousefi, *Image Binarization using Otsu Thresholding Algorithm* (2015). https://doi.org/doi:10.13140/RG.2.1.4758.9284
21. D. Dendrinos, On the fuzzy nature of shadows, academia.edu. Mar. 2017
22. X. Huang, G. Hua, J. Tumblin, L. Williams, What characterizes a shadow boundary under the sun and sky? in *2011 International Conference on Computer Vision*, (Barcelona, Spain, IEEE, 2011), pp. 898–905. https://doi.org/doi:10.1109/ICCV.2011.6126331
23. C. Giraud-Carrier, R. Vilalta, P. Brazdil, Introduction to the special issue on meta-learning, Mach. Learn. **54**, 187 (2004)
24. M. Axisa, M. Demicoli, L. Mule'Stagno, Analysing the effects of thin object shading on PV sources: a dual approach combining outdoor and laboratory solar simulator experimentation, Energies **17**, 2069 (2024). https://doi.org/doi:10.3390/en17092069
25. T. Kumar, K. Verma, A theory based on conversion of RGB image to gray image, Int. J. Comput. Appl. **7**, 0975 (2010). https://doi.org/doi:10.5120/1140-1493.
26. S. Chandran, *Color Image to Grayscale Image Conversion* (2010), p. 199 https://doi.org/10.1109/ICCEA.2010.192
27. K. Mirylenka, G. Giannakopoulos, T. Palpanas, SRF: a framework for the study of classifier behavior under training set mislabeling noise, in *Advances in Knowledge*

Discovery and Data Mining, edited by N. Tan, S. Chawla, C.K. Ho, J. Bailey, Lecture Notes in Computer Science 7301 (Springer Berlin Heidelberg, 2012), pp. 109–121

28. J. F. Hair, *Research Methods for Business* (John Wiley & Sons, 2007). Available: https://archive.org/details/researchmethodsf0000unse_j4k9/page/358/mode/2up?q=moderate

Cite this article as: Matthew Axisa, Luciano Mule'Stagno, Marija Demicoli, Quantifying the effect of shadow formation on photovoltaic sources under thin object shading: an image analysis approach, EPJ Photovoltaics **16**, 17 (2025), https://doi.org/10.1051/epjpv/2025005